International Journal of Hydrogen Energy 118 (2025) 343–355

Contents lists available at ScienceDirect

International Journal of Hydrogen Energy

journal homepage: www.elsevier.com/locate/he

Burning ammonia–hydrogen mixtures in a staged combustor with high efficiency and low pollutant emissions

Alessandro Piscopo [a,b,c], Lorenzo Giuntini [a,b], Chiara Novelli [a,b], Ward De Paepe [c], Axel Coussement [a,b], Alessandro Parente [a,b,d,*]

[a] Université Libre de Bruxelles,École Polytechnique de Bruxelles, Aero-Thermo-Mechanics Laboratory, Avenue Franklin Roosevelt 50, Brussels, 1050, Belgium
[b] Université Libre de Bruxelles and Vrije Universiteit Brussel, Brussels Institute for Thermal-Fluid Systems and Clean Energy (BRITE), Avenue Franklin Roosevelt 50, Brussels, 1050, Belgium
[c] University of Mons, Thermal Engineering & Combustion Unit, Rue de l'Epargne 53, Mons, 7000, Belgium
[d] WEL Research Institute, Avenue Pasteur 6, Wavre, 1300, Belgium

ARTICLE INFO

Keywords:
Ammonia
Hydrogen
Combustion
Surrogate model
NO_x emissions
Polynomial Chaos Expansion
Reynolds-averaged Navier–Stokes

ABSTRACT

The urgent need to reduce our dependence on fossil fuels requires a massive transition toward renewable energy. Yet, directly using renewable electricity is challenging for heavy industries needing huge amounts of heat and high process temperatures, conditions realistically achievable only through combustion. In this scenario, sustainable fuels offer a promising pathway for decarbonizing hard-to-abate sectors, and fuel mixtures with varying compositions are expected to become the norm. To support this shift, fuel-flexible technologies will be crucial to ensure steady operation without affecting efficiency and pollutant emissions. Among various carbon-free fuels, ammonia has gained considerable attention as a hydrogen carrier due to its more favorable storage requirements. However, its low reactivity and tendency to produce NO_x and N_2O requires tailored fueling strategies to improve flame stability and limit emissions. Blending ammonia with hydrogen addresses reactivity issues, while staged combustion may be effective for achieving low pollutants and high efficiency. A novel burner design combining a stagnation-point reverse-flow (SPRF) chamber with air staging showed promising low emissions in initial tests; therefore, further investigation on the performance of this combustor prototype is needed. In this work, we tested such a novel design on a much wider operating space in terms of equivalence ratio in the rich region, operating pressure and ammonia/hydrogen composition in the fuel. Computation Fluid Dynamics (CFD) simulations were performed to characterize the combustor performance over this operating space. A surrogate model based on Polynomial Chaos Expansions (PCE) was then developed and trained on CFD data to capture the highly non-linear relationships between the operating parameters and pollutant emissions. After validation, the PCE model was used to identify optimal regions for low-emission combustion. The results demonstrated that the proposed combustor design is robust with stable NO_x + N_2O emission below 100 ppm_v at 16% O_2 over a wide range of input parameters, thereby offering the operational flexibility needed to boost the use of green fuels in the industry.

1. Introduction

In the search for clean combustion alternatives to fossil fuels, green hydrogen and ammonia have gained significant attention due to their potential for carbon-free energy production [1]. Hydrogen, which can be directly produced from water via electrolysis, presents challenges in storage and transportation owing to its low density, necessitating costly measures such as compression or cryogenic cooling [2]. Ammonia, on the other hand, offers a higher volumetric energy density, simplifying storage and transport. However, its synthesis involves additional steps compared to hydrogen, introducing complexity and efficiency losses [3], in addition to its toxicity that explains the need to get rid of unburned ammonia in the flue gases [4].

When used as fuels, hydrogen and ammonia face distinct combustion challenges. Pure ammonia flames suffer from low stability, slow reaction kinetics, and the risk of high NO_x and N_2O emissions [5,6]. In contrast, hydrogen's high reactivity can cause either flashback in premixed flames [7] or extremely high temperatures in non-premixed flames, thus enhancing thermal NO_x formation [8]. The ambitious

* Corresponding author at: Université Libre de Bruxelles,École Polytechnique de Bruxelles, Aero-Thermo-Mechanics Laboratory, Avenue Franklin Roosevelt 50, Brussels, 1050, Belgium.
E-mail address: Alessandro.Parente@ulb.be (A. Parente).

https://doi.org/10.1016/j.ijhydene.2025.03.099
Received 15 January 2025; Received in revised form 25 February 2025; Accepted 6 March 2025
Available online 19 March 2025

goal of the research community is to tackle all these challenges, ensuring that carbon-free fuels can rapidly replace fossil ones, thereby accelerating the energy transition. In this transition, various fuels are expected to contribute to the energy mix, bringing variability in composition. Among these, ammonia–hydrogen blends are likely to become increasingly common. Therefore, fuel-flexible burners will be essential to maintain continuous operation, especially during periods of fuel supply fluctuations, enabling the seamless integration of varying fuel mixtures in industrial burners. Among the technologies available, flameless combustion [6,9] and staged combustion [10–13] have shown the most promise, providing high efficiency, fuel-flexibility, and low pollutant emissions. However, even these advanced combustion systems can struggle to ensure proper and stable operation for varying fuel mixtures. As such, numerical simulations are essential for devising design improvements and identifying optimal operating conditions.

In this context, Computational Fluid Dynamics (CFD) represents a valuable tool to analyze the burner behavior emissions-wise and find appropriate improvement for reaching low NO_x. Nevertheless, CFD simulations are computationally intensive, particularly when investigating a broad spectrum of operating conditions. To overcome this limitation, reduced-order models (ROMs) have garnered attention for their ability to provide rapid yet reliable approximations of complex systems. Among these approaches, Chemical Reactor Networks (CRNs) have been successfully applied to real combustion systems to estimate pollutant emissions, emulating the actual combustor behavior through interconnected ideal 0D/1D reactors [14–16]. Other ROM types are those based on Gaussian Process Regression (GPR). These models have been typically employed to build digital twins of actual combustion systems by reconstructing the field of key quantities of interest over the whole combustor volume [17,18]. Additionally, multi-fidelity frameworks have recently emerged, combining costly high-fidelity data with computationally inexpensive low-fidelity models to create ROMs that leverage the advantages of both [19–22]. Among these surrogate modeling techniques, Polynomial Chaos Expansion (PCE) [23–25] stands out as a powerful approach for combustion applications. Beyond its capability to efficiently approximate complex input–output relationships, PCE enables the integration of uncertainty quantification (UQ) and sensitivity analysis, providing valuable insights into the impact of operating parameters on system performance. This makes it particularly useful for identifying robust designs and optimal operating conditions that minimize pollutant emissions. Despite their methodological differences, all these surrogate models share a common feature: they can be trained on a limited set of operating points and then used to reconstruct complex system behavior, allowing for rapid exploration of a wide range of conditions. This is particularly important considering that NO_x and N_2O emissions are highly sensitive to key operating parameters such as equivalence ratio, fuel composition, and pressure [26,27].

In the present study, a staged combustor adapted for ammonia combustion is investigated. A CFD model of the original combustor geometry, named A-type design, was validated against experimental data collected at the combustor's outlet as presented in [13]. After validation, two novel geometries were devised, resulting in the B-type and C-type designs. The former consists of a reduction in the size of the external diameter of the primary air nozzle, while the latter retains this modification and includes four additional holes in the sleeve's wall, where the air is injected gradually. This is further explained in Section 2. These combustor prototypes were tested on a few selected operating points, showing promising results on the NO emissions, therefore highlighting the need for further investigation. The aim of this work is to conduct a systematic parametric analysis to assess pollutant emissions on a much wider operating space, providing results that can be generalized to other staged combustor designs. CFD simulations are performed to characterize the combustor's performance for varying equivalence ratios, fuel composition, and operating pressure. Then, a PCE-based surrogate model is developed to capture the highly nonlinear relationships between the operating parameters and NO_x and N_2O emissions, which, to the best of the author's knowledge, has been barely done in the literature. After validation, the surrogate model is used to identify optimal regions for low-emission combustion. The results of this study will provide practical and techno-economic information to design and operate next-generation combustors for fuel-flexible, low-NO_x and low-N_2O ammonia/hydrogen oxidation.

The paper is structured as follows: Section 2 introduces the three combustor geometries; Section 3 describes the CFD model, and validates its accuracy. A single combustor type among those initially presented is then selected based on preliminary performance results. In Section 4, a CFD dataset comprising 175 RANS simulations is generated for the chosen combustor design, covering a wide range of operating conditions. Section 5 details the development and training of a PCE-based surrogate model using the CFD dataset. Results are presented and analyzed in Section 6, and conclusions are summarized in Section 7.

2. ULB modified stagnation-point reverse-flow combustor

The SPRF combustor developed at the Université Libre de Bruxelles, first introduced in a study by Giuntini et al. [13], is considered in this work and depicted in Fig. 1, with indications of the flow direction and a detailed view of the modifications implemented in the B-type and C-type cases. Initially designed for natural gas combustion in a single fuel-lean stage with air injection for exhaust gas dilution, the original combustor referred to as the A-type design was re-conceptualized for staged, rich-lean, ammonia oxidation. This adaptation led to the development of two additional configurations labeled as B-type and C-type designs.

In comparison to the A-type, where the primary air is injected at approximately 20 m/s, the B-type and C-type designs feature a reduced diameter of the primary air nozzle, increasing the inlet velocity to approximately 90 m/s. This modification allows for improving the mixing within the first combustion stage. Additionally, the C-type design incorporates a further modification with the introduction of four holes in the wall separating the secondary air from the products of the first stage. Through these holes, air is injected, resulting in the so-called continuously-staged SPRF combustor [13].

3. CFD model

Reynolds-Averaged Navier–Stokes (RANS) simulations were carried out using Ansys Fluent v22.1 with a pressure-based solver. Turbulence was modeled using the Realizable $k-\epsilon$ approach with enhanced wall treatment [13]. The reacting source term was closed using the Partially Stirred Reactor (PaSR) model with the integral-based formulation for the mixing time, setting $C_{mix} = 0.1$ [13]. The chemical time scale was determined based on the slowest reacting species among O_2, H_2O, N_2, H_2, and NH_3, as outlined in [28]. The Shrestha mechanism [29] was selected to model NH_3/H_2 oxidation [13]. Radiation effects were modeled using the Discrete Ordinate (DO) model, coupled with the Weighted-Sum of Gray Gases (WSGG) model for gas properties. A User-Defined Function (UDF) was used to adjust the WSGG band coefficients based on the work of Bordbar et al. [30] to account for the absence of methane in the fuel, for which the model was initially developed in Fluent, and to adapt the model to different fuel compositions.

A 2D axisymmetric mesh comprising 53,000 quadrilateral and triangular cells was employed. This mesh ensured a $y^* < 1$ across all surfaces. Simulation convergence was verified by monitoring residuals, the heat balance, and the stability of NO_x emissions at the outlet. The computational time to achieve convergence in each simulation was about 7 days on 20 CPUs.

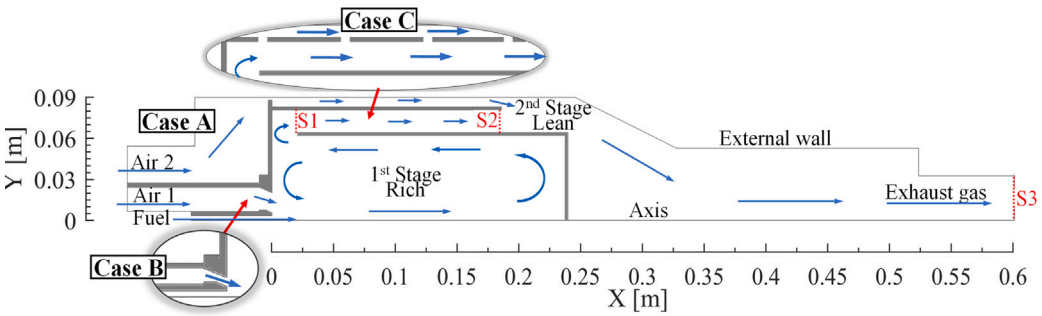

Fig. 1. 2D axisymmetric representation of the ULB modified SPRF combustor. The modifications made to the original geometry (Case A) are indicated as Case B and Case C, respectively. The arrows highlight the flow directions, red dotted lines indicate the sampling zones (S1 = first stage, S2 = second stage, and S3 = outlet).
Source: Adapted from [13].

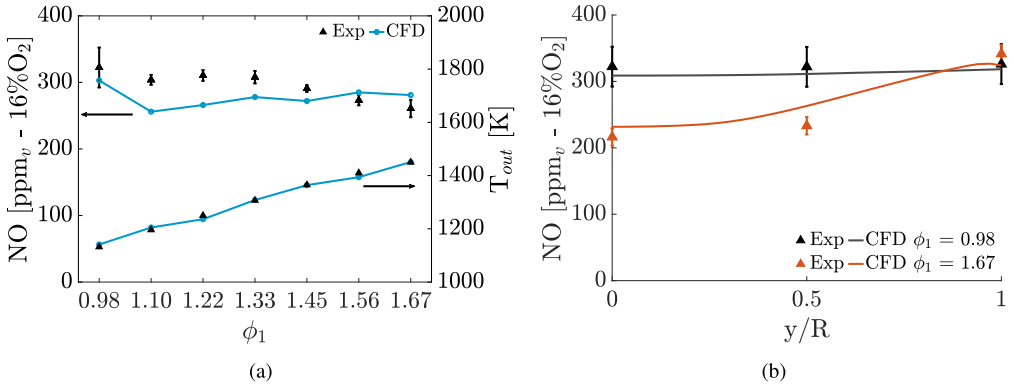

Fig. 2. Performance of the CFD model in predicting experimental data collected on the A-type design: (a) NO emissions (left) and outlet temperature (right) at different rich equivalence ratios (ϕ_1), and (b) NO emissions along the radial direction of the burner at $\phi_1 = 0.98$ and $\phi_1 = 1.67$.
Source: Adapted from [13].

3.1. Model validation

The availability of experimental data on flue gas composition and temperature for the A-type geometry facilitated the validation of the CFD model described above. A comprehensive validation, including the determination of the optimal C_{mix} value of 0.1 for the PaSR combustion model, the selection of the Realizable $k-\epsilon$ turbulence model, and the adoption of the Shrestha kinetic mechanism, is detailed in [13]. However, for the reader's convenience, a complete excerpt from this validation is also presented in Fig. 2 to demonstrate the CFD model's ability to predict experimental data of NO and temperature at the combustor's outlet. In Fig. 2(a), the model shows relatively good agreement with experimental NO emissions across different operating conditions, with an average relative error of 9%. For the exhaust gas temperature, the average relative error goes down to 0.57%, across the entire range of first-stage equivalence ratios (ϕ_1) investigated. Additionally, for the two extreme conditions, i.e., $\phi_1 = 0.98$ and $\phi_1 = 1.67$, experimental NO emissions were also collected at the exit pipe along the radial direction, with $y/R = 0$ indicating the combustor axis and $y/R = 1$ the pipe's wall. As visible in Figure Fig. 2(b), the CFD model can capture both the absolute NO value and the relatively flat radial distribution of experimental NO at the outlet.

3.2. Combustor performance assessment

Initially, 56 RANS-CFD simulations were conducted with the objective of evaluating and identifying the optimal configuration between the B-type and C-type cases.[1] The simulations covered a range of operational conditions, with fuel compositions set as either pure ammonia or a 70/30 mol% ammonia/hydrogen blend. Operating pressures of 1 bar (atmospheric pressure) and 2 bar were considered, and the equivalence ratio in the first fuel-rich stage (ϕ_1) was varied between 1 and 1.6.

A thermal power input of 20 kW was used for simulations at 1 bar, while the power was scaled to 40 kW for simulations at 2 bar. Scaling the power, and consequently, the mass flows, ensured consistent jet velocities within the combustor across different pressures, maintaining optimal fluid-dynamics conditions and isolating the effect of pressure on pollutant emissions. Further details are provided in Section 4.

In all cases, air was preheated to 900 K, and the global equivalence ratio was set to achieve an outlet temperature of 1200 K. For the C-type design, the amount of secondary air evenly injected through the four holes is such to guarantee stoichiometric conditions at the last (i.e., fourth) hole, ensuring that the ammonia/hydrogen mixture coming from the first, fuel-rich, stage is completely converted under rich-to-stoichiometric conditions. As reported in Tables 1 and 2, an increase in pressure is associated with a reduction in emissions across all cases. Fig. 3 illustrates the trends for both designs. The N_2O emissions exhibit a monotonic increase with ϕ_1, with the C-type design demonstrating lower emissions than the B-type design for all conditions. Instead, the NO_x emission exhibits a V-shaped trend with respect to ϕ_1, with the minimum that shifts depending on the operating condition. It is noteworthy that the minimum of the emissions occurs at a lower ϕ_1 for pure ammonia cases (i.e., $\phi_1 = 1.15$ for case B at 1 and 2 bar, and $\phi_1 = 1.15/1.2$ for case C at 1 and 2 bar, respectively) in comparison to

[1] Following the findings of [13], the original combustor, referred to as the A-type design, was found to be not optimized for ammonia combustion, therefore shifting the attention only to the B- and C-type geometries.

Table 1
NO_x emissions (in ppm_v, dry-basis, sampling zone S3) at 16% O_2 for Cases B and C as a function of the equivalence ratio in the first region (ϕ_1). Data are presented for operating pressures of 1 and 2 bar, with fuel compositions of 0% H_2 (pure NH_3) and 30% H_2.

		CASE B				CASE C			
		0% H_2		30% H_2		0% H_2		30% H_2	
	ϕ_1	1 bar	2 bar	1 bar	2 bar	1 bar	2 bar	1 bar	2 bar
NO_x	1	1033	873	1428	828	1033	873	1428	828
	1.15	74	70	240	112	60	78	267	282
	1.2	269	102	76	83	79	46	92	94
	1.25	510	283	226	118	175	91	57	39
	1.3	898	466	460	375	304	148	84	62
	1.45	1545	926	1147	892	606	277	368	159
	1.6	1847	1196	1718	1291	650	315	474	210

Table 2
N_2O emissions (in ppm_v, dry-basis, sampling zone S3) at 16% O_2 for Cases B and C as a function of the equivalence ratio in the first region (ϕ_1). Data are presented for operating pressures of 1 and 2 bar, with fuel compositions of 0% H_2 (pure NH_3) and 30% H_2.

		CASE B				CASE C			
		0% H_2		30% H_2		0% H_2		30% H_2	
	ϕ_1	1 bar	2 bar	1 bar	2 bar	1 bar	2 bar	1 bar	2 bar
N_2O	1	0	0	0	828	0	0	0	0
	1.15	0	0	0	0	0	0	0	0
	1.2	4	0	0	0	0	0	0	0
	1.25	16	0	0	0	0	0	0	0
	1.3	28	0	5	6	6	0	0	0
	1.45	107	26	29	32	29	2	6	0
	1.6	205	67	74	81	38	2	0	0

cases with 30% H_2 in the fuel (i.e., $\phi_1 = 1.2$ for case B at 1 and 2 bar, and $\phi_1 = 1.25$ for case C at 1 and 2 bar). Thus, with the addition of hydrogen to the fuel mixture, the NO_x minimum shifts toward higher equivalence ratios. To explain this behavior, we must remind that, in staged combustors, total NO_x emissions result from the combined contributions of all combustion stages, and the minimum occurs when overall NO_x production is minimized. Moreover, it is crucial to remind that ammonia plays a dual role in NO_x chemistry: it reduces NO_x under fuel-rich conditions but promotes NO_x formation under fuel-lean conditions. Therefore, in the first, fuel-rich stage, a higher availability of NH_3 is desirable to enhance NO_x reduction. In contrast, in the second, fuel-lean stage, minimizing NH_3 availability helps suppress NO_x formation. However, these two effects are inherently linked. Indeed, operating the first stage at a highly fuel-rich condition minimizes NO_x production but results in significant NH_3 slip to the second stage, where it subsequently promotes NO_x formation. On the other hand, operating the first stage at low NH_3 slips (i.e., by either operating with ϕ_1 close to 1 or by increasing the H_2 share at the expense of NH_3 in the fuel mixture) leads to substantial NO_x formation in that stage but ensures nearly complete NH_3 consumption, minimizing NO_x formation in the second stage. Overall, the NO_x minimum is achieved by balancing NO_x formation in both stages. This optimization involves finding a balance where the first stage produces sufficiently low NO_x while also ensuring that the second stage receives minimal NH_3, thereby preventing excessive NO_x formation in that stage. Consequently, with the addition of hydrogen to the fuel mixture (for instance, from 0%H_2 to 30%H_2 as shown in Fig. 3), as the availability of NH_3 in the first stage reduces, the first-stage equivalence ratio must increase to maintain this balance, thereby shifting the NO_x minimum toward higher ϕ_1 values.

In the majority of the examined conditions, the C-type configuration exhibits lower values of emissions with respect to the B-type, with the minimum of NO_x at 38 ppm_v at $\phi_1 = 1.25$, $p_o = 2$ bar, 30% H_2 in the fuel for C-type, and 70 ppm_v at $\phi_1 = 1.15$, $p_o = 2$ bar, pure ammonia for B-type, respectively. Overall, the C-type combustor exhibits lower emissions across a broader range of conditions in comparison to the B-type, thereby affording greater flexibility in the selection of operating conditions. This results in a more robust, stable, and suitable design for industrial applications. Consequently, the C-case is selected for the subsequent parametric analysis.

4. CFD data generation

For the selected C-case configuration, a systematic parametric analysis was conducted to evaluate the impact of three key operating parameters on NO_x and N_2O (also denoted as N_xO_x) emissions: the equivalence ratio in the first stage (ϕ_1), the hydrogen mole fraction in the fuel mixture (x_{H_2}), and the system's operating pressure (p_o in bar).

To ensure proper operation of the SPRF combustor, internal velocities were held constant as pressure varied. This was achieved by scaling the mass flow rates proportionally with pressure, following the relation: $\dot{m}_i = \frac{p_o}{p_o^0} \cdot \dot{m}_i^0$. For instance, the fuel flow rate in [kg/s] was calculated as:

$$\dot{m}_{fuel} = p_o/p_o^0 \cdot \dot{m}_{fuel}^0 = p_o/p_o^0 \cdot P_{th}^0/LHV_{mix} \tag{1}$$

with $P_{th}^0 = 20$ kW at $p_o^0 = 1$ bar, and LHV_{mix} which depends on the lower heating value of the fuel mixture. The air mass flow rate in the first, fuel-rich, stage (denoted as $\dot{m}_{air,1}$) was calculated based on the equivalence ratio ϕ_1 as follows:

$$\dot{m}_{air,1} = \phi_1 \cdot (F/A)_{st} \cdot \dot{m}_{fuel} \tag{2}$$

where $\left(\frac{F}{A}\right)_{st}$ is the stoichiometric fuel-to-air ratio, which depends on the fuel composition.

Regarding the air injected through the holes in the sleeve wall (between surfaces S1 and S2 in Fig. 1) and denoted as $\dot{m}_{air,2}$, this flow was evenly distributed across the four holes to achieve an equivalence ratio of 1 at the final (fourth) hole, as already mentioned in the previous section and detailed in [13]. We remind that this is a key feature of the C-type design, as it ensures that ammonia is continuously oxidized under rich conditions, which is crucial to mitigate pollutant formation. The total air flow rate ($\dot{m}_{air,tot}$) was determined through a global energy balance to maintain an outlet temperature of 1200 K in each simulation, ensuring consistent thermal conditions across all cases, as discussed in [13]. Finally, the remaining air injected in the third region (between surface S2 and S3 in Fig. 1) was computed as:

$$\dot{m}_{air,3} = \dot{m}_{air,tot} - \dot{m}_{air,1} - \dot{m}_{air,2} \tag{3}$$

Initially, the multivariate joint distribution of the three input parameters, assuming a uniform distribution for each of them, was sampled

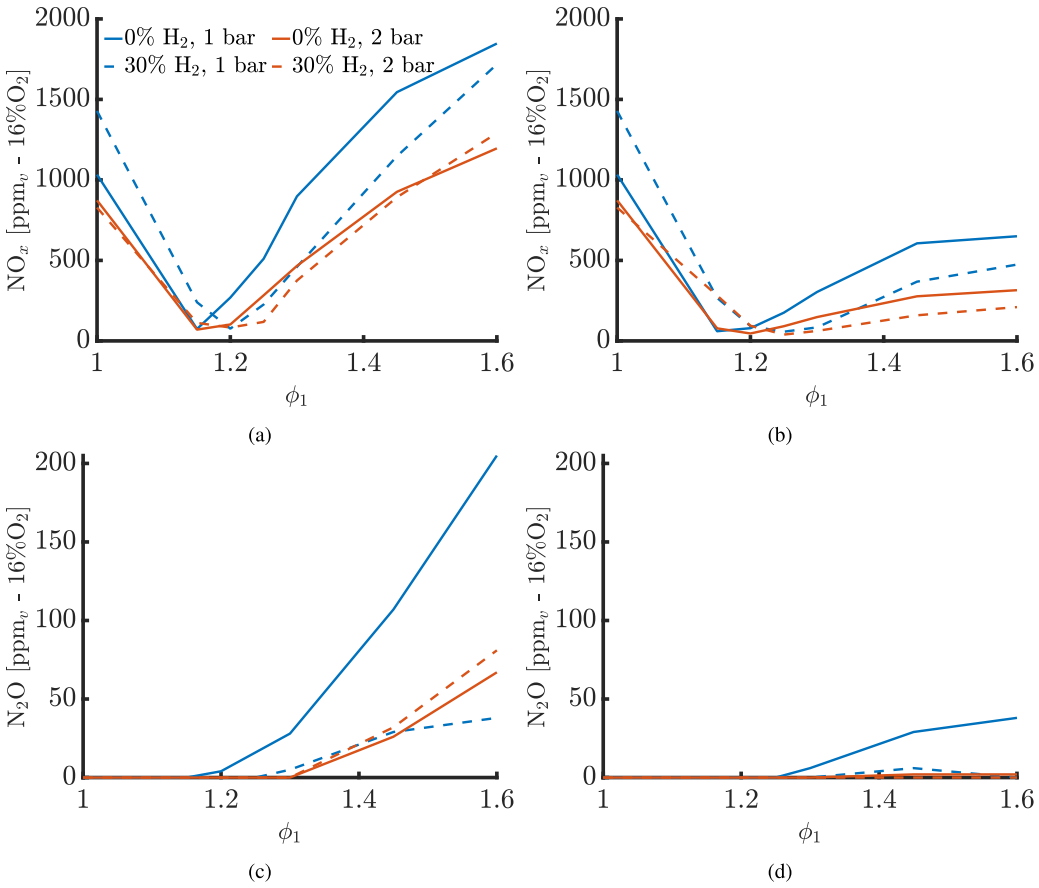

Fig. 3. NO_x (top) and N_2O (bottom) emissions (in ppm_v, dry-basis, sampling zone S3) at 16% O_2 as a function of rich equivalence ratio (ϕ_1) for Case B (a,c) and Case C (b,d), respectively.

using Latin Hypercube Sampling (LHS), resulting in 70 evaluation points on which CFD simulations were then conducted. A uniform distribution was chosen for the input parameters to ensure each value within the specified range had an equal probability of being selected, allowing for uniform sampling across the entire operational range. Indeed, since the input parameters are not inherently uncertain, the uniform distribution represents a methodological choice to systematically explore the parameter space. The lower and upper bounds of the three operating parameters were defined as:

$$\phi_1 \in [1, 1.6], \quad p_o \in [1, 3], \quad x_{H_2} \in [0, 0.75] \tag{4}$$

To further refine the design space, additional points were added using a two-step approach: first, to take advantage of the 28 simulations already performed in Section 3.2 for the C-type design, they were added with 6 additional points at the design space corners, resulting in a total of 34 new points. Next, an adaptive sampling algorithm was implemented to focus sampling on critical regions requiring further refinement. For this analysis, only NO_x were considered for the output. This algorithm first scales the input coordinates $x_{i,k}$ and the corresponding outputs Y_i between 0 and 1, as follows:

$$x'_{i,k} = \frac{x_{i,k} - x_k^{min}}{x_k^{max} - x_k^{min}}, \quad Y'_{i,} = \frac{Y_i - Y^{min}}{Y^{max} - Y^{min}} \tag{5}$$

where, i indexes the sample points from 1 to n, while k iterates over the three operating parameters. The normalized Euclidean distance between two consecutive sample points was then computed as r_{ij} and used to calculate the gradient between their corresponding output values:

$$r_{ij} = \sqrt{\sum_{k=1}^{3} (x'_{i,k} - x'_{j,k})^2}, \quad g_{ij} = \frac{|Y_i - Y_j|}{r_{ij}}, \quad \forall i \neq j \tag{6}$$

The minimum and maximum of the Euclidean distance and the gradient were then retained for setting a threshold on both quantities:

$$r_{threshold} = r_{min} + \lambda_r(r_{max} - r_{min}), \quad g_{threshold} = g_{min} + \lambda_g(g_{max} - g_{min}), \tag{7}$$

where λ_r, λ_g are user-defined coefficients determining the strictness of the threshold, ranging between 0 (threshold = minimum value) and 1 (threshold = maximum value). Finally, new samples x_i^{new} were generated midway between existing $\mathbf{x_i}$ and $\mathbf{x_j}$ points, subject to the threshold conditions. This approach ensured that new points were added in regions with higher gradients while maintaining sufficient distance between samples to prevent overlap. The design space was then updated, and new CFD simulations were iteratively performed until a satisfactory degree of approximation (indicated by λ_r and λ_g) of the system response surface was achieved. In total, the final design space comprised 175 CFD simulations for the selected C-type design, as shown in Fig. 4. Such a high number of sampling points was necessary because of the large dimension of the design space and the highly non-linear nature of the NO_x and N_2O emissions response to the input parameters.

5. Polynomial chaos expansion surrogate model

The 175 RANS-CFD simulations conducted across varying ϕ_1, p_o and x_{H_2} values served as high-fidelity data to train and validate a surrogate model based on Polynomial Chaos Expansion (PCE). The goal of the PCE model was used to efficiently reconstruct a response surface for NO_x emissions at the combustor's outlet, with the three operating parameters as inputs. This was further extended for N_2O emissions, as it is a greenhouse gas with an important global warming potential [31].

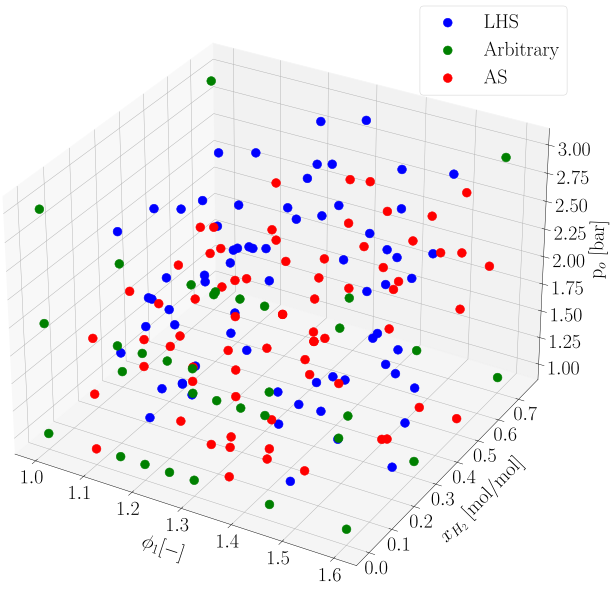

Fig. 4. Three-dimensional grid of the 175 CFD simulations conducted in this work, colored by the different sampling methods employed (LHS = Latin Hypercubic Sampling, Arbitrary = boundary samples + Section 3.2 simulations, AS = Adaptive Sampling). (For interpretation of the references to colour in this figure legend, the reader is referred to the web version of this article.)

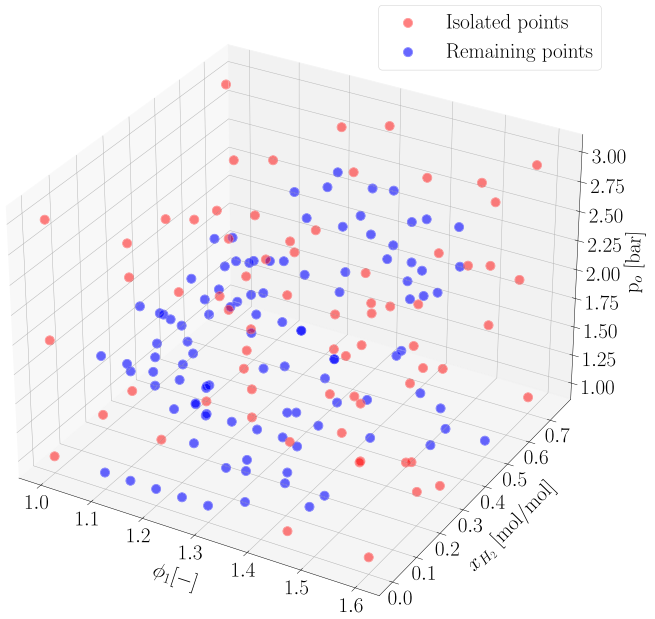

Fig. 5. Three-dimensional grid representing the 175 CFD simulations conducted in this study, colored according to their isolation score. The red points, accounting for 40% of the total, represent the most isolated samples, while the remaining 60% are shown in blue. Test points are selected from the blue samples. (For interpretation of the references to colour in this figure legend, the reader is referred to the web version of this article.)

In the PCE framework, the output quantity of interest Y is decomposed into many (potentially infinite) deterministic terms:

$$Y = \sum_{k \in N} a_k \Psi_k(x) \tag{8}$$

For practical application the infinite-dimensional representation is truncated to a smaller number of coefficients, where p_o is set as small as possible while maintaining a sufficiently good approximation.

$$Y(x) \approx \sum_{k=0}^{P} a_k \Psi_k(x) \tag{9}$$

where a_k are coefficients that must be estimated during the PCE training, Ψ_k represents the multivariate orthogonal polynomials of degree k, while $x = (x_1, x_2, x_3)$ are the input parameters [24]. The convergence of the model was assessed by comparing the mean of the observation to the order zero coefficient.

To facilitate the training process, input and output data were scaled between 0 and 1, as reported in Eq. (5). The full dataset was split into training and test samples by using a train/test split ratio of 80/20% (i.e., 140/35 CFD points). Due to the rather large dimension of the design space, to ensure effective training of the surrogate model, certain critical points, specifically the most isolated ones, were intentionally retained within the training dataset and excluded from testing. In this regard, an isolation score based on the Euclidean distance between the points was calculated and assigned to each sample, and those showing the highest scores were retained within the training set to maximize coverage and avoid extrapolation. The corresponding points are shown in Fig. 5.

As for the PCE order, it was selected to achieve a satisfactory R^2 score value to effectively fit both the training dataset and the unseen test points. After validation, the PCE model was employed for global sensitivity analysis using Sobol indices for the NO_x and N_2O models. Both first-order and total-order Sobol indices were computed. The first-order index measures the direct effect of each individual input parameter on the output response as follows:

$$S_i = \frac{V_{x_i}(E_{x_{\sim i}}(Y(\mathbf{x}) \mid x_i))}{V(Y(\mathbf{x}))}, \tag{10}$$

where $x_{\sim i}$ represents the set of all input parameters except x_i, $Y(\mathbf{x})$ is the model response, $V(Y(\mathbf{x}))$ is the total variance of the output, and $V_{x_i}(E_{x_{\sim i}}(Y(\mathbf{x}) \mid x_i))$ is the variance of the expected response when x_i changes, considering the other inputs fixed.

The total-order index considers the full effect of the input parameters on the output as follows:

$$S_{T_i} = \frac{E_{x_{\sim i}}(V_{x_i}(Y(\mathbf{x}) \mid x_{\sim i}))}{V(Y(\mathbf{x}))}, \tag{11}$$

where $V_{x_i}(Y(\mathbf{x}) \mid x_{\sim i})$ is the variance of the response with respect to x_i, holding the other parameters fixed, and $E_{x_{\sim i}}$ denotes the expected value over all values of the other input parameters.

6. Techno-economic analysis

Afterwards, the PCE-based model was utilized to evaluate the operating cost of the combustor in relation to the level of emitted pollutants. This approach aims to provide a tool for conducting a simplified techno-economic analysis of the current burner, which can also be extended to other combustor geometries. To do this, a cost function was defined, as the sum of two terms: the pressure-related cost, which accounts for the energy required by the air compressor to increase the pressure from 1 bar to a specified level above the atmospheric pressure, and the fuel-related cost, representing the expense of the fuel mixture (hydrogen and ammonia). For a better generalization to other combustors, both costs were normalized by the thermal power input of the burner, $P_{th} = \dot{m}_{fuel} \cdot LHV_{mix}$ expressed in kW. For the former, the power required by the compressor was adapted from [32] and can be expressed as:

$$C_{pr} = \frac{1}{P_{th}} \left(\frac{\dot{m}_{air,tot} \cdot c_p^{\text{air}} \cdot T_{\text{in}}^{\text{air}}}{\eta_{\text{comp}}} \right) \cdot \left(\beta^{\frac{\gamma-1}{\gamma}} - 1 \right) \cdot \xi_{\text{elec}} \cdot f \cdot t \tag{12}$$

where $\dot{m}_{air,tot}$ kg/s is the total mass flow rate of air compressed and fed to the combustor, $c_p^{\text{air}} = 1005\,\text{J/(kg} \cdot \text{K)}$ is the specific heat capacity of air, $T_{\text{in}}^{\text{air}} = 300\,\text{K}$ is the inlet air temperature, $\eta_{\text{comp}} = 0.8$ is the efficiency

of the compressor assumed constant[2] [32]; β is the compression ratio defined as $\beta = p_{out}/p_{in}$ with $p_{in} = 1$ bar; $\gamma = 1.4$ is the adiabatic index, $\xi_{elec} = 0.28$ €/kWh is the price of the electricity required to power the compressor [33], $f = \frac{1}{1000}$ kWh/Wh is a conversion factor, and $t = 3600$ s that corresponds to 1 h of operation.

For the fuel cost, prices per kilogram from the literature are used: for ammonia, $\xi_{NH_3} = 0.852$ €/kg [34], and for hydrogen, $\xi_{H_2} = 6.21$ €/kg [35]. The fuel cost is calculated as:

$$C_{fuel} = \frac{\dot{m}_{fuel}}{P_{th}} \left(M_{H_2} x_{H_2} \xi_{H_2} + M_{NH_3} x_{NH_3} \xi_{NH_3} \right) \cdot t \quad (13)$$

where $\dot{m}_{fuel}$ is the molar flow rate of the fuel in kmol/s, M_i is the molar mass of species i in kg/kmol, and x_i is its molar fraction in the fuel.

We invite the reader to refer to the supplementary materials attached to the main manuscript, where a sensitivity analysis on fuel price variability is included. This analysis consists of three additional scenarios: (1) a 50% increase in H_2 price and a 50% decrease in NH_3 price, (2) a 50% decrease in H_2 price and a 50% increase in NH_3 price, and (3) similar increase/decrease for both H_2 and NH_3 at the same time.

7. Results and discussion

This section presents the results. First, the CFD-predicted NO_x and N_2O emissions were evaluated as functions of the unreacted hydrogen-to-ammonia ratio in the combustion products from the first stage. Controlling this ratio is crucial to limiting emissions. Such analysis was carried out for both the B- and C-case designs, to compare the performance of different combustors. Subsequently, the PCE model was used to reconstruct the field of NO_x and N_2O emissions across the whole range of operating conditions, before proposing the techno-economic analysis. All emissions in this study were normalized to the reference 16% O_2 content (typical for staged combustion applications) in the dried flue gases and expressed in ppm_v.

7.1. Preliminary considerations to minimize pollutant emissions

To minimize outlet emissions, it is crucial to suppress pollutant formation across all combustion stages. This task is generally straightforward in the first combustion zone, as pollutant formation is strongly reduced under fuel-rich conditions for ammonia–hydrogen blends. Typically, ϕ_1 values above 1.15, when only ammonia is present in the fuel, are sufficient to ensure low NO_x and N_2O formation in the first stage, although this value may vary slightly (± 0.05) depending on the burner configuration. Furthermore, since ammonia is the key species for reducing pollutants under fuel-rich conditions, ammonia–hydrogen blends generally require higher ϕ_1 values to achieve similar outcomes.

Regarding the subsequent combustion zone(s), the formation of NO_x and N_2O depends on the amount of unreacted ammonia slipping from the first stage and the equivalence ratio in the secondary combustion zone(s), i.e., ϕ_i with $i > 1$. Indeed, a higher ammonia concentration in the first-stage flue gases increases the likelihood of pollutant generation downstream. Therefore, high ammonia decomposition in the first, rich, stage, and thus a high $(H_2/NH_3)_1$ ratio is crucial to limit pollutant formation in the following stage(s). Simultaneously, a lean equivalence ratio within the secondary combustion zone(s) (either global or also in local pockets) promotes pollutant formation if any ammonia is present. Summing up, to minimize pollutants effectively, it is essential to maintain low pollutants in the first stage, with a high $(H_2/NH_3)_1$ ratio, while ensuring $\phi_i \geq 1$ for all subsequent stages, i.e., for all $i > 1$.

Fig. 6 illustrates the relationship between the hydrogen-to-ammonia molar ratio at the outlet of stage 1 and the NO_x and N_2O emissions at the combustor outlet, obtained in the CFD simulations, with data color-coded by the rich equivalence ratio (ϕ_1). The performance analysis, introduced in Section 3.2, concludes that the C-type configuration significantly reduces N_xO_x emissions and demonstrates better stability under varying operating conditions. For what concerns the NO_x, when comparing the $(H_2/NH_3)_1$ ratios of the two designs, distinct trends are observed: both show a parabolic shape with a minimum at the center, but the curve for the C-type combustor is flatter, and the region of acceptable NO_x emissions (below 70 ppm_v at 16% O_2) is much broader than that for the B-type design. Specifically, the lowest NO_x values occur for hydrogen-to-ammonia ratios of $(H_2/NH_3)_1 \in [3\times10^2 - 3\times10^3]$ for the B-type and $\in [10^2 - 5\times10^3]$ for the C-type.

Since both combustors are identical in the first stage, the performance in the first stage is nearly the same for both geometries and all conditions. Therefore, the superior performance of the C-type design over the B-type is attributed to better control of the equivalence ratio in stages downstream of the first. Specifically, the presence of four subsequent secondary air injections, all having $\phi_1 \geq 1$, ensures lower pollutant formation in the secondary combustion zones. In addition, the gradual heat release also helps in reducing the pollutant formation. To illustrate this, Fig. 7(a) retakes the heat release in the B- and C-type combustor, for the case with $\phi_1 = 1.45$, pure ammonia at 1 bar. The heat is released in a more distributed mode than in the B-type, where the release is more localized with a higher intensity than the C-type. Indeed, in the former, the maximal heat release, which is observed after the second stage, is higher than the C-type, 37.8 W against 7.6 W. Thanks to this gradual heat release, the C-type combustor operates under milder conditions, therefore lowering the flame intensity. This results in reduced local temperatures, which hinder reaction pathways that lead to ammonia decomposition into NO_x. Fig. 7(b) depicts the NO reduction by the kinetic reaction $NH_2 + NO \rightarrow N_2 + H_2O$, showing a similar pattern to Fig. 7(a). As discussed for the heat release, case C shows enhanced deNO_x reactions with the gradual injection of air through the dilution holes, allowing for lower emissions at the outlet.

Recalling Fig. 6, additional considerations can be made by examining the shape of the NO_x curves. As already anticipated, a key factor for ensuring low NO_x emissions is promoting the decomposition of ammonia into hydrogen, thus resulting in a high $(H_2/NH_3)_1$ ratio while maintaining a high enough ϕ_1. Indeed, for $\phi_1 \sim [1 - 1.15]$, a lot of NO_x are already produced in the first stage, contributing to the overall emissions at the outlet. Points corresponding to $\phi_1 \sim 1$ are concentrated in the high $(H_2/NH_3)_1$ ratio region, as ammonia slip is minimal at this value of ϕ_1. For higher values of ϕ_1, specifically in the range of $\phi_1 \sim [1.45 - 1.6]$, the C-type combustor exhibits lower NO_x emissions compared to the B-type, which reaches its peak NO_x values under these conditions. Therefore, the optimal range for the rich equivalence ratio to minimize NO_x emissions appears to be between $[1.15 - 1.45]$.[3] The advantage of the C-type design over the B-type is its ability to maintain relatively low NO_x emissions even in the higher ϕ_1 regions. When operating to the right of the parabola minimum, much of the NO_x is produced in the first stage, while to the left, the NO_x results primarily from the second stage. In the plateau region near the minimum, emissions from both stages are minimized, leading to the lowest overall NO_x emissions.

Regarding N_2O emissions, the trends reported in Fig. 6 are different. Although not explicitly shown, there is no substantial formation of N_2O in the first, rich, stage across all conditions investigated. This is because N_2O formation is suppressed at lower ϕ_1 values compared to

[2] Assuming constant compressor efficiency is valid since, in our system, the total air mass flow scales linearly with pressure to maintain optimal combustor velocities. Consequently, the compressor operates along the bisector of a typical compressor map (compression ratio vs. mass flow rate), aligning with efficiency isolines.

[3] It should be noted that the conditions considered for the B-case design are limited to pressures of $p_o \in [1-2]$ bar and hydrogen content $x_{H_2} \in [0-0.3]$, as this data was part of the preliminary study reported in Section 3.2. However, this constraint does not affect the overall trends.

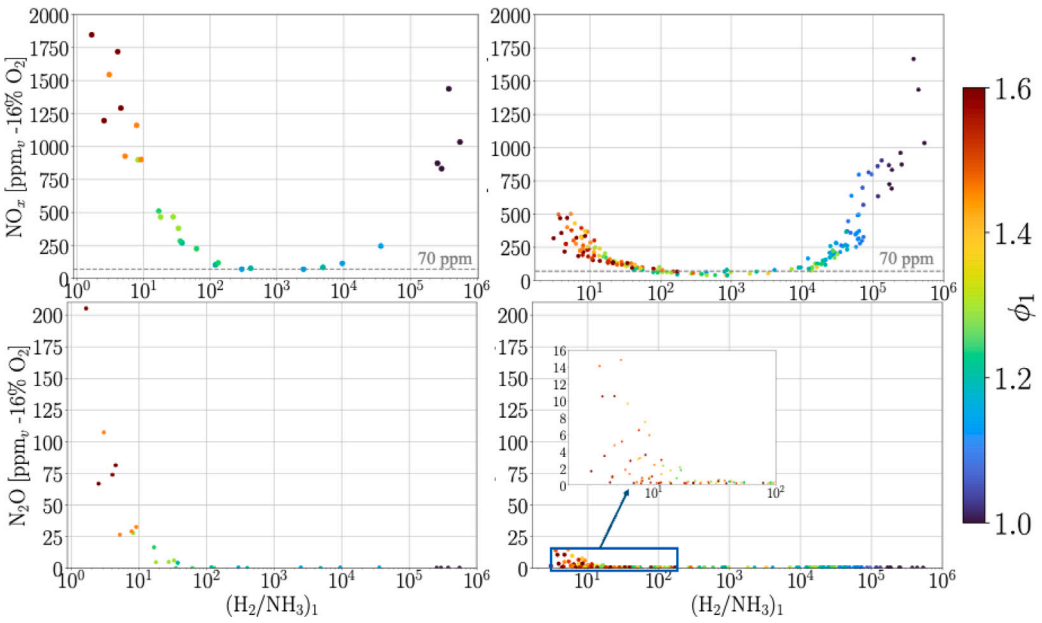

Fig. 6. NO_x (top) and N_2O (bottom) emissions (in ppm_v, dry-basis, sampling zone S3) normalized at 16% O_2 as a function of the ratio between hydrogen and ammonia at the outlet of the first stage, i.e., $(H_2/NH_3)_1$ where subscript 1 indicates the sampling zone S1. The data is colored by the value of the rich equivalence ratio ϕ_1, for the B-case (left) and C-case (right). The X-axis is set to a logarithmic scale. A close-up of the low N_2O values for low $(H_2/NH_3)_1$ ratios in the C-type combustor is also shown.

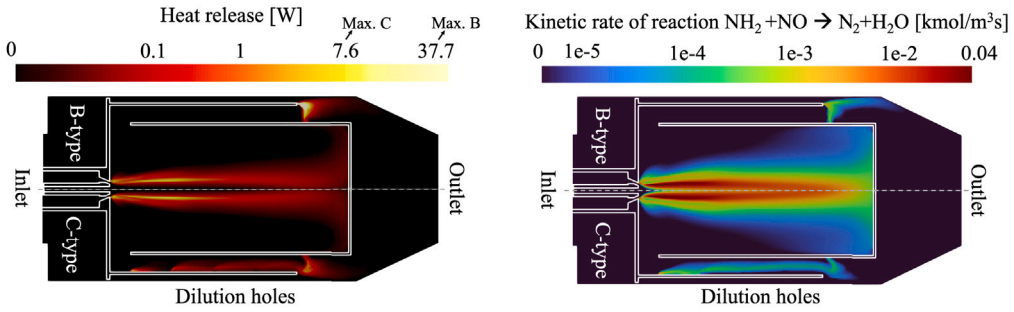

Fig. 7. Mirror view contours of the B-type (top) and C-type (bottom) combustors for (a) the heat release and (b) the kinetic rate of a key NO reduction reaction. The operating conditions considered are $\phi = 1.45$, $x_{H_2} = 0$ and $p_o = 1$ bar are considered. The maximal heat release is also highlighted for the B-type (37.7 W) and C-type (7.6 W); both color bars use the log scale.

NO_x, resulting in a trend that lacks the right branch of the parabolic shape. On the left branch, instead, corresponding to low ammonia decomposition and high ϕ_1, a significant amount of ammonia reacts in the secondary zone(s). This results in some N_2O emissions at the combustor outlet, particularly for the B-type design, which operates with a single, fuel-lean, secondary stage. In contrast, the continuously staged configuration characteristic of the C-type design effectively keeps N_2O emissions below 15 ppm_v under all conditions investigated.

7.2. NO_x -PCE and N_2O-PCE model development

The prediction performance of the PCE-based surrogate model is shown in the parity plot in Fig. 8. The NO_x PCE order was set to 4, resulting in a regression performance evaluated via R^2 score of 97% on the training data and 94% on the test points. A convergence study to determine the optimum polynomial order of the NO_x- and N_2O-PCE models was carried out and is reported in the supplementary materials. Additionally, the parity plot in Fig. 8(a) provides insight into the distribution of NO_x emissions at the burner outlet, indicating that most operating points fall below 200 ppm_v for the presented combustor design, underscoring its effectiveness in maintaining low emission levels across various conditions. The PCE model for N_2O emissions was also configured with an order of 4, achieving an R^2 score of 96% on the training dataset and 92% on the testing dataset. The narrow emission range of N_2O, which lies between 0 and 38 ppm, with most points close to 0 ppm_v can be observed in Fig. 8(b). This also means that little discrepancies, in the order of 0.1 to 1 ppm_v, between PCE and CFD predictions, can affect the R^2 score value, which is a bit lower compared to the NO_x-PCE for both training and testing, though the model portrays satisfactory agreement.

7.3. Global sensitivity analysis

Fig. 9 shows the normalized first-order and total-order Sobol indices, calculated following Eqs. (10) and (11), respectively. These indices indicate the influence on the NO_x and N_2O of each operating parameter. For what concerns NO_x emissions, the equivalence ratio in the first combustion stage is the main contributor with indices of 92% and 76%, for the first and total order, respectively. As for the fuel composition, expressed as hydrogen content, it shows a quite marginal first-order effect of about 1%, while it becomes more important, i.e., about 12.5%, when considering also higher-order effects,

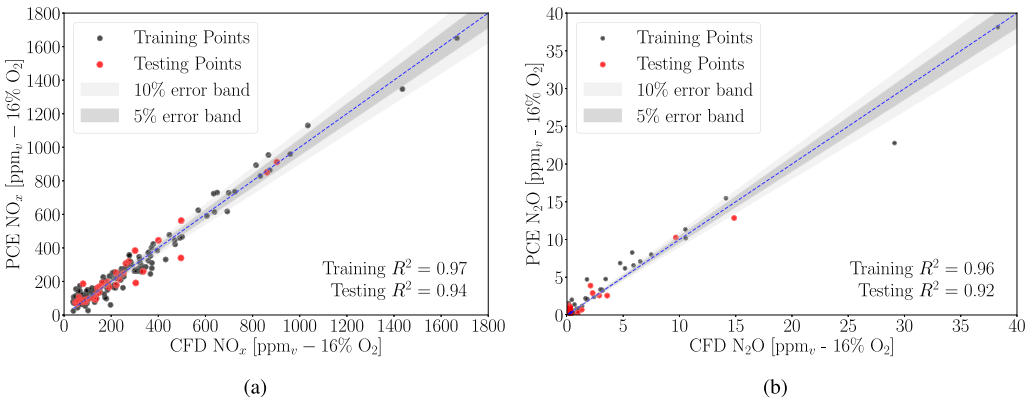

Fig. 8. PCE-estimated vs CFD-estimated (a) NO_x and (b) N_2O emissions at the combustor outlet (in ppm_v, dry-basis, sampling zone S3) for the training and testing datasets. Training points are in black, while testing points are in red. A 5% and 10% error bands are also included. The training and testing R^2 score values are also reported. (For interpretation of the references to colour in this figure legend, the reader is referred to the web version of this article.)

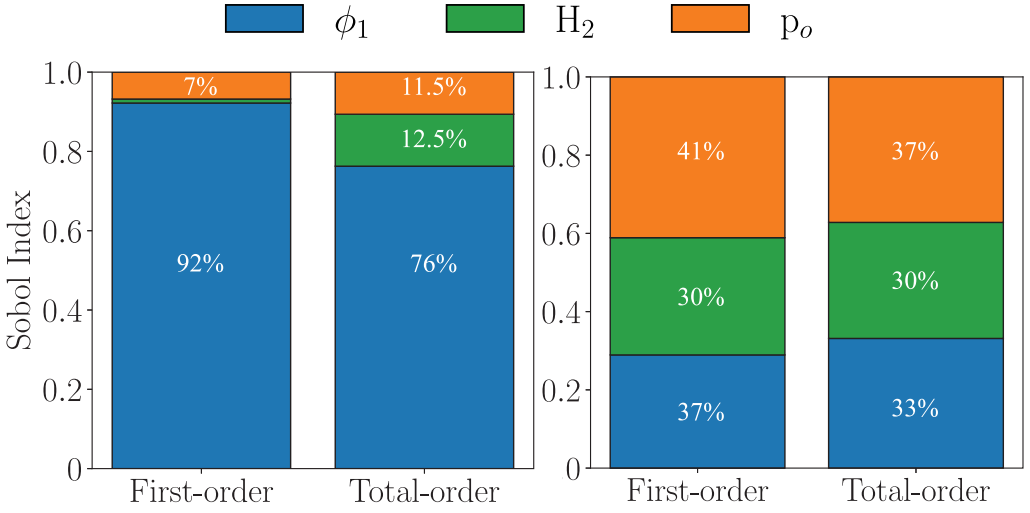

Fig. 9. Normalized first-order and total-order Sobol indices for the NO_x (left) and N_2O (right) emissions, for the three operating parameters considered in this work: rich equivalence ratio, hydrogen molar fraction in the fuel, and operating pressure.

thereby indicating strong interactions with the other two input parameters. The operating pressure, instead, shows a relatively constant contribution of 7% and 11.5% for first-order and total-order Sobol indices, respectively, indicating that pressure is relatively decoupled from the other parameters.

For the N_2O Sobol indices, the pressure takes over with a rather high first-order contribution of 41% and a total-order contribution of 37%. The equivalence ratio in the first rich stage and the hydrogen content have similar importance to the variability of the output. Their first-order indices rank up to 37% and 30%, respectively, and their total order to 33% and 30%.

7.4. Optimal conditions for low pollutant emissions

Fig. 10 presents the NO_x emissions predicted by the PCE model across the entire design space for three different pressure levels. The quasi-vertical orientation of the isolines confirms that ϕ_1 has a stronger influence on NO_x levels than the hydrogen molar fraction (x_{H_2}), consistent with the Sobol indices. The primary effect of x_{H_2} is to shift the minimum NO_x emissions toward higher ϕ_1. This occurs because increasing x_{H_2} reduces the ammonia available for abating pollutants in the first combustion stage, necessitating a higher ϕ_1 to achieve similar emission reductions. For example, at p_o = 1 bar, the minimum shifts obliquely from $\phi_1 = 1.22$ for $x_{H_2} = 0$ to $\phi_1 = 1.55$ for $x_{H_2} = 0.75$.

As also anticipated in Fig. 6, we can confirm that, if the fuel composition is properly controlled, the most stable region lies between about $\phi_1 = 1.15$ and $\phi_1 = 1.45$, providing NO_x between 0 and 200 ppm_v across the various pressure levels. Conversely, operating at $\phi_1 \sim 1$ results in the highest NO_x at the outlet, due to the high amount of NO_x already produced at the first stage and this effect is boosted at high x_{H_2}. When increasing the pressure, instead, the NO_x globally decreases, with smaller regions of high NO_x and larger regions below 100 ppm_v values.

The analysis of N_2O emissions is presented in Fig. 11, focusing on p_o = 1 bar, as higher pressures offer limited additional insights. At elevated pressures, N_2O emissions are near zero across most conditions, except in the region around $\phi_1 = 1.6$ and $x_{H_2} = 0$. At 1 bar, N_2O emissions reach a peak value of 38 ppm_v, while the predicted peak values at 2 bar and 3 bar decrease significantly to 2.4 and 1.8 ppm_v, respectively. This trend remarks on the crucial role of pressure, as previously suggested by the Sobol indices analysis for N_2O.

In summary, pressure is a key parameter for limiting pollutant emissions. As the operating pressure increases, three-body pressure-sensitive reactions, such as H + OH + M = H_2O + M and H + O_2 +

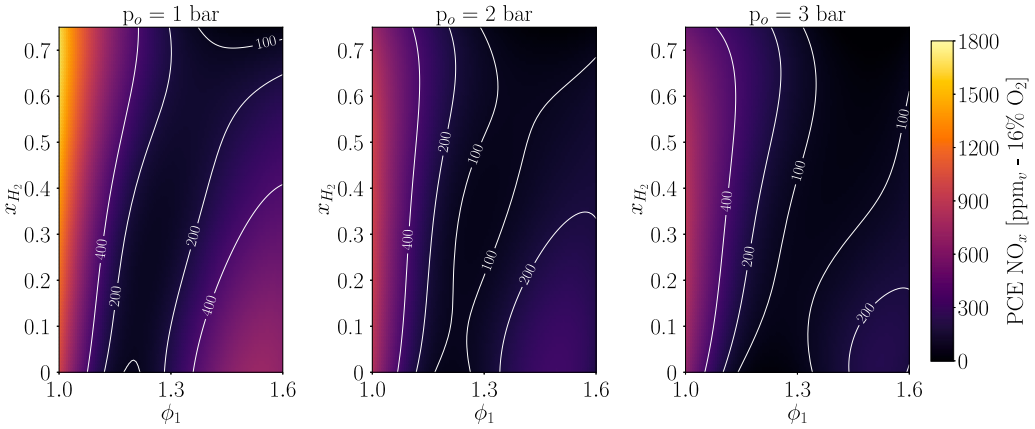

Fig. 10. Contour plots of PCE predicted NO_x emissions (normalized at 16% O_2) as a function of the equivalence ratio in the first combustion stage (ϕ_1) and the hydrogen content in the fuel mixture (x_{H_2}) at three fixed pressures: 1, 2, and 3 bar. Isolines are shown at selected NO_x emission levels: 100, 200, and 400 ppm_v.

M = HO_2 + M, are enhanced [36]. The first reaction acts as a chain-terminating step, while the second competes with the production of OH and O from H + O_2 = OH + O, producing less reactive HO_2 radicals. The net effect is a reduction in the concentration of reactive O and OH radicals, accompanied by a relative increase in the H/O ratio. This alteration in the radical pool concentration and composition has two effects:

1. In the first stage, the H/O ratio, already high due to fuel-rich conditions, is further increased by the high pressure, boosting the conversion of NH_3 to H_2 [36] via the NH_i + H cascade. As a result, the $(H_2/NH_3)_1$ ratio of the flue gas entering the secondary combustion zones increases. This leads to less ammonia available for oxidation in the subsequent fuel-lean stage, eventually reducing the formation of fuel-NO_x and N_2O.
2. Across the entire burner, and especially in the fuel-lean zones where oxygenated radicals (O, OH) are more concentrated, the increase in the H/O ratio due to increased pressure weakens the main N_xO_x formation pathways, particularly those involving NH_i + O/OH, ultimately reducing pollutant emissions [36].

Following this logic, although the effect of pressure tends to flatten as p_o increases further [37], ultra-high $(H_2/NH_3)_1$ ratios can be achieved for pressures above 10–20 bar (e.g., in gas turbines). This results in ultra-low NO_x and N_2O production in the secondary stage(s), particularly flattening the left branch of the curves in Fig. 6. This enables low-emission operation across a wide range of conditions, thereby enhancing the robustness and flexibility of the combustor.

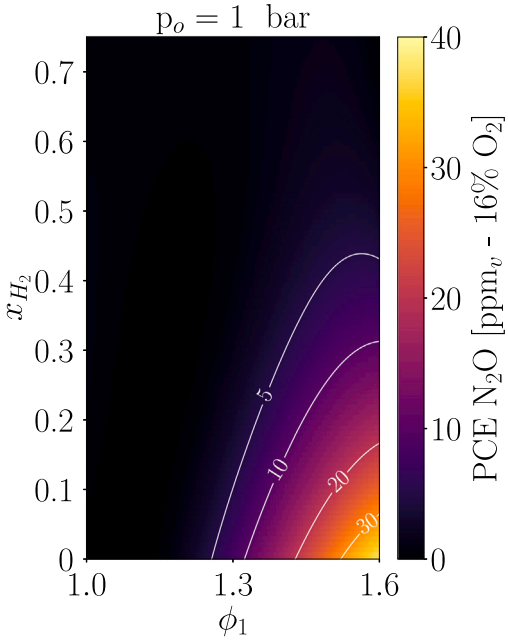

Fig. 11. Contour plot of PCE predicted N_2O emissions (in ppm_v, dry-basis, sampling zone S3) normalized at 16% O_2 as a function of the equivalence ratio in the first combustion stage (ϕ_1) and the hydrogen content in the fuel mixture (x_{H_2}) at 1 bar. Isolines are shown at selected N_2O emission levels: 5, 10, 20, and 30 ppm_v.

7.5. Techno-economic analysis

Fig. 12 presents the Kernel Density Estimate (KDE) plot of the PCE-predicted NO_x emissions as a function of ϕ_1 and x_{H_2}, over the range considered in this study, for three different pressure levels. It is displayed against the estimated hourly operating cost, calculated as the sum of Eqs. (12) and (13). This visualization highlights the distribution of NO_x emissions for various operating conditions and their associated costs. At a fixed pressure level, the operating cost increases approximately linearly with the hydrogen content in the fuel blend. Regions with high density in the KDE plot correspond to stable operating windows, where small variations in operating conditions result in minimal changes in emissions.

Interestingly, the total cost rises more at increasing pressure than increasing the hydrogen content in the fuel. However, it is worth noting that the stable region with low NO_x shifts from high hydrogen to low hydrogen content, as the pressure increases, allowing to partially compensate the increased cost due to pressure with the reduced cost of the fuel.

Additionally, higher pressures expand the stable region with low pollutant emissions, causing the kernel distribution to become more concentrated at lower NO_x levels. For instance at p_o = 1 bar, NO_x peaks at approximately 1500 ppm_v, with a relatively narrow stable region that settles to around 200 ppm_v and a cost of 0.175 €h/kW; whereas, at 2 bar and 3 bar, NO_x peak remains below 1000 ppm_v, with a wider stable operating window around 150 ppm_v and 100 ppm_v, respectively corresponding to 0.23 €h/kW at 2 bar and 0.266 €h/kW at 3 bar.

However, it is important to emphasize that these results may be sensitive to fluctuations in fuel prices, which is likely given the global uncertainties surrounding the future energy market. The impact of fuel price variability is illustrated in Fig. 12 using arrows, where their thickness represents the intensity of the effect. The arrows are only depicted in Fig. 12 at p_o = 1 bar, but the same considerations apply for the other

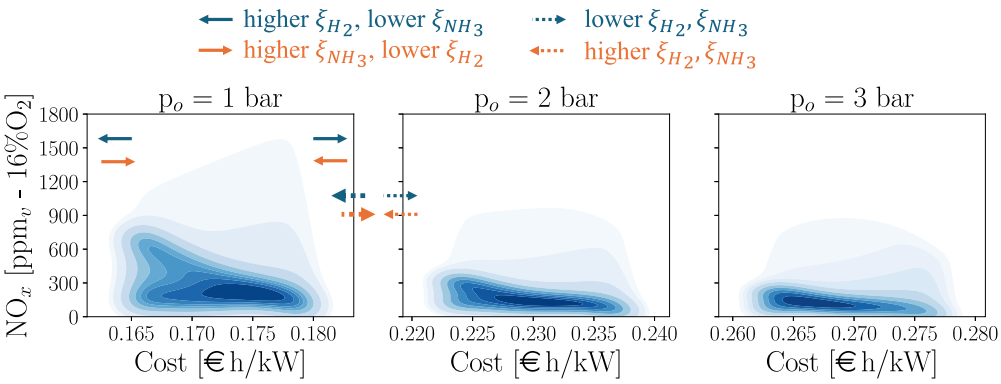

Fig. 12. KDE plots of PCE-predicted NO_x emissions (in ppm_v, dry-basis, sampling zone S3) normalized at 16% O_2 as a function of the hourly cost for three selected pressures: 1 bar, 2 bar, and 3 bar, with darker regions indicating higher density areas. The reference prices of ammonia and hydrogen are set at $\xi NH_3 = 0.852$ €/kg and $\xi_{H_2} = 6.21$ €/kg. The impact of fuel price variations on the reference KDE plots is represented by the arrows.

pressure levels as well as for N_2O in Fig. 13. Initially, scenarios with opposite variations in fuel prices are considered. First, if the price of hydrogen increases while the price of ammonia decreases with respect to the reference scenario, the minimum cost decreases, and the maximum cost increases at a given pressure, thus expanding the KDE distributions. This enhances the competitiveness of pressurization, as increasing the operating pressure while maintaining an ammonia-dominated blend results in similar costs to a system at $p_o = 1$ bar with a higher hydrogen fraction in the blend. In this case, burning ammonia-dominated blends becomes more favorable at higher pressures. Conversely, if ammonia prices increase while hydrogen prices decrease, the minimum cost rises, and the maximum cost decreases, as indicated by the arrows. Depending on the magnitude of these price changes, the kernel density estimate (KDE) may collapse into a single vertical line or even invert its shape, meaning that lower costs correspond to higher H_2 content in the fuel. This inversion occurs when the energy price, expressed in €/MJ, is the same for both ammonia and hydrogen, i.e., when $\frac{\xi_{H_2}}{LHV_{H_2}} = \frac{\xi_{NH_3}}{LHV_{NH_3}}$. Finally, we examine a scenario in which both fuel prices increase or decrease simultaneously. When prices rise, fuel costs become more dominant compared to pressurization costs, making higher operating pressures more advantageous. Conversely, if both prices decrease, fuel costs play a less significant role in the total cost, making an operating pressure of 1 bar more favorable, as electricity costs for compression become the primary cost driver. We invite the reader to check the supplementary materials for further details.

Similar trends can be observed for the KDE plots of N_2O emissions shown in Fig. 13. As previously mentioned, N_2O emissions decrease significantly with increasing pressure, reaching stable values close to 0 ppm_v at pressures of 2 and 3 bar. The highest N_2O emission values occur at low operating costs, corresponding to low pressure and low hydrogen content in the fuel blend, as indicated by the spread kernel distribution. Similar to NO_x, the stable region of N_2O emissions shifts from high hydrogen content to low hydrogen content as pressure increases, partially offsetting the increased cost due to pressure with a reduction in fuel costs. However, while the increased operating cost at 3 bar may be justified for reducing NO_x emissions, this is not the case for N_2O. At 2 bar, N_2O emissions already fall close to 0 ppm_v, making higher pressures and their associated costs unnecessary.

In conclusion, operating the combustor at pressures above atmospheric levels can be advantageous but comes at a cost. Systems that inherently operate under pressure, such as gas turbines, can leverage these benefits effectively. In contrast, for atmospheric systems, the increased cost may not be justified. Therefore, to ensure low NO_x and N_2O, it is crucial to ensure steady input conditions or to mitigate input fluctuations through accurate control systems that maintain the combustor within the stable, low-emission, operating window.

Other than that, optimizing the combustor design remains critical to achieving a sufficiently wide operating window with minimal pollutant emissions. In this context, the continuously staged design of the C-type configuration provides a promising geometric improvement over traditional two-stage burners. This superiority was evidenced in the comparison between the B-type and C-type burners (see previous sections), where the latter demonstrates significantly better performance in reducing pollutant formation.

8. Conclusions

This paper analyzed the operating robustness of a novel design of the ULB Stagnation-Point Reverse-Flow (SPRF) burner across a broad range of operating conditions. The study focused on three key parameters: the rich equivalence ratio in the first combustion stage (ϕ_1), the hydrogen molar fraction in the fuel blend (x_{H_2}), and the operating pressure (p_o), examining their effects on pollutant emissions. To achieve this, a surrogate model based on Polynomial Chaos Expansion (PCE) was developed using data from 175 2D RANS simulations, allowing the reconstruction of pollutant emission response surfaces as functions of the input parameters.

The NO_x-PCE model revealed that NO_x emissions peaked at ϕ_1 near 1, driven by significant fuel-NO_x production in the first combustion stage. At mid-range ϕ_1 values, NO_x levels were minimal, as NO_x formation was reduced across all combustion stages. At higher ϕ_1 values, the substantial slip of unreacted ammonia from the first combustion stage led to elevated NO_x and N_2O emissions in subsequent stages, resulting in high overall pollutant levels. Regarding N_2O emissions, the combustor demonstrated robust performance, with the highest N_2O level of 38 ppm_v observed at ϕ_1 near 1.6 with 0% H_2, at 1 bar. Increasing the pressure to 2 or 3 bars effectively reduced N_2O emissions to near zero, highlighting the significant impact of operating pressure on N_2O mitigation.

In line with the Sobol indices, this analysis confirmed that ϕ_1 had a significant impact on NO_x variability, while N_2O emissions remain low over the whole domain of operating conditions considered. The combustor demonstrated robustness in maintaining low-NO_x emissions across a broad range of ϕ_1, hydrogen content, and operating pressure. Specifically, the stable ϕ_1 region for achieving emissions below 70 ppm_v was identified between 1.15 and 1.45. Increasing the hydrogen content extended this acceptable ϕ_1 range up to 1.6, an effect that was further amplified by operating at higher pressures.

This study concludes by presenting a combined NO_x and N_2O techno-economic analysis, which provides an indicative hourly cost as a function of the operating conditions. The findings highlight the environmental benefits of operating at high pressures, which result in reduced pollutant emissions, albeit with increased operational costs. This trade-off underscores the importance of balancing environmental and economic considerations in the design and operation of combustion systems.

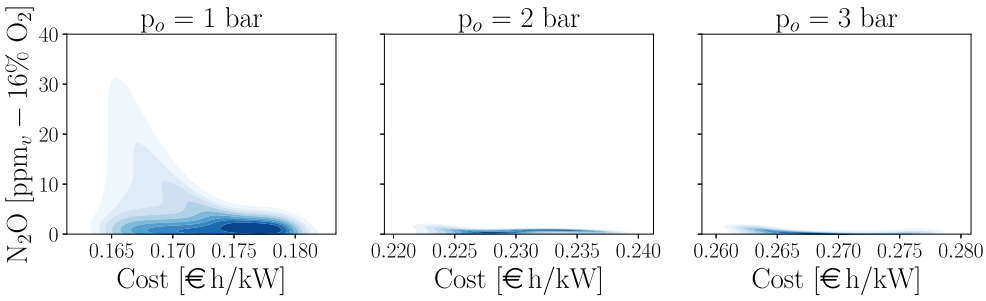

Fig. 13. KDE plots of PCE-predicted N_2O emissions (in ppm_v, dry-basis, sampling zone S3) normalized at 16% O_2 as a function of the hourly cost for three selected pressures: 1 bar, 2 bar, and 3 bar, with darker regions indicating higher density areas.

Future work will focus on investigating the combustor's response to variations in operating conditions, aiming to develop a dynamic surrogate model capable of capturing the system's transient behavior during transitions between steady states. Such a model is particularly relevant given the increasing demand for combustion systems to operate under transient conditions rather than steady states to ensure the flexibility needed to accommodate fluctuating energy demands and varying fuel supply/price.

CRediT authorship contribution statement

Alessandro Piscopo: Writing – original draft, Visualization, Methodology, Investigation, Data curation, Conceptualization. **Lorenzo Giuntini:** Writing – original draft, Visualization, Methodology, Investigation, Conceptualization. **Chiara Novelli:** Data curation. **Ward De Paepe:** Writing – review & editing, Supervision. **Axel Coussement:** Supervision, Software, Resources. **Alessandro Parente:** Writing – review & editing, Supervision, Resources, Methodology, Conceptualization.

Declaration of competing interest

The authors declare that they have no known competing financial interests or personal relationships that could have appeared to influence the work reported in this paper.

Acknowledgments

A. Piscopo, W. De Paepe and A. Parente acknowledge the financial support of the Fonds National de la Recherche Scientifique (FRS-FNRS) for the Hydrogenate Project (T004222F; Funder ID: 10.13039/501100002661). A. Parente and C. Novelli acknowledge research funding from the European Union's Horizon Europe research and innovation program under grant agreement No 101072779. L. Giuntini acknowledges the financial support of SPF Economie on the H2GridTwin project. The authors thank Salvatore Iavarone and Ruggero Amaduzzi for their valuable advice on the development of the PCE-based surrogate model. This research was funded, in whole or in part, by the FNRS, Belgium. A CC BY licence is applied to the AAM arising from this submission, in accordance with the grant's open access conditions.

Appendix A. Supplementary data

Supplementary material related to this article can be found online at https://doi.org/10.1016/j.ijhydene.2025.03.099.

References

[1] Yan Y, Liu Z, Liu J. Computational analysis of ammonia-hydrogen blends in homogeneous charge compression ignition engine operation. Process Saf Environ Prot 2024;190:1263–72. http://dx.doi.org/10.1016/j.psep.2024.07.102, URL https://www.sciencedirect.com/science/article/pii/S0957582024009479.

[2] Muhammed NS, Haq MB, Al Shehri DA, Al-Ahmed A, Rahman MM, Zaman E, Iglauer S. Hydrogen storage in depleted gas reservoirs: A comprehensive review. Fuel 2023;337:127032. http://dx.doi.org/10.1016/j.fuel.2022.127032, URL https://www.sciencedirect.com/science/article/pii/S001623612203856X.

[3] Fatehi M, Renzi M. Modelling and development of ammonia-air non-premixed low NO_x combustor in a micro gas turbine: A CFD analysis. Int J Hydrog Energy 2024;88:1–10. http://dx.doi.org/10.1016/j.ijhydene.2024.09.071, URL https://www.sciencedirect.com/science/article/pii/S0360319924037819.

[4] Wen M, Liu H, Zhang S, Yue Z, Cui Y, Ming Z, Feng L, Yao M. A study of ammonia combustion induced by high reactivity fuel based on optical diagnostics and chemical kinetic analyses. Combust Flame 2025;272:113896. http://dx.doi.org/10.1016/j.combustflame.2024.113896, URL https://www.sciencedirect.com/science/article/pii/S0010218024006059.

[5] Meng X, Zhao C, Qin M, Zhang M, Dong D, Long W, Bi M. Study on chemical kinetics and NO behaviors in pre-chamber jet-induced ignition mode with ammonia. Fuel Process Technol 2023;250:107876. http://dx.doi.org/10.1016/j.fuproc.2023.107876, URL https://www.sciencedirect.com/science/article/pii/S0378382023002242.

[6] Ariemma GB, Sorrentino G, Ragucci R, de Joannon M, Sabia P. Ammonia/Methane combustion: Stability and NO_x emissions. Combust Flame 2022;241:112071. http://dx.doi.org/10.1016/j.combustflame.2022.112071, URL https://www.sciencedirect.com/science/article/pii/S0010218022000906.

[7] Jowkar S, Shen X, Olyaei G, Morad MR. Hydrogen-enriched propane combustion in a lean premixed burner: LES study on flashback, emissions, and combustion instability. Fuel 2025;381:133377. http://dx.doi.org/10.1016/j.fuel.2024.133377, URL https://www.sciencedirect.com/science/article/pii/S0016236124025262.

[8] Jamshidiha M, Kamal M, Cafiero M, Coussement A, Parente A. Experimental and numerical characterization of hydrogen combustion in a reverse-flow micro gas turbine combustor. Int J Hydrog Energy 2024;55:1299–311. http://dx.doi.org/10.1016/j.ijhydene.2023.11.243, URL https://www.sciencedirect.com/science/article/pii/S0360319923059888.

[9] Giuntini L, Frascino L, Ariemma GB, Sorrentino G, Galletti C, Ragucci R. Modeling of ammonia MILD combustion in systems with internal recirculation. Combust Sci Technol 2023;195(14):3513–28.

[10] Okafor EC, Somarathne KDKA, Hayakawa A, Kudo T, Kurata O, Iki N, Kobayashi H. Towards the development of an efficient low-NO_x ammonia combustor for a micro gas turbine. PROCI 2019;37(4):4597–606.

[11] Pugh D, Valera-Medina A, Bowen P, Giles A, Goktepe B, Runyon J, Morris S, Hewlett S, Marsh R. Emissions Performance of Staged Premixed and Diffusion Combustor Concepts for an NH_3/Air Flame With and Without Reactant Humidification. J Eng Gas Turbine Power 2021;143(5).

[12] Srinivasarao M, Sorrentino G, de Joannon M, Reddy VM. Pure ammonia flames with high thermal intensities through fuel and air staging under extreme rich-to-lean conditions. Proc Combust Inst 2024;40(1):105241. http://dx.doi.org/10.1016/j.proci.2024.105241, URL https://www.sciencedirect.com/science/article/pii/S1540748924000518.

[13] Giuntini L, Novelli C, Kamal MM, Cafiero M, Galletti C, Coussement A, Parente A. Continuously-staged NH_3 oxidation in a stagnation-point reverse-flow combustor for low NO_x emissions. Proc Combust Inst 2024;40(1):105674. http://dx.doi.org/10.1016/j.proci.2024.105674, URL https://www.sciencedirect.com/science/article/pii/S1540748924004826.

[14] Nguyen TH, Park J, Sin C, Jung S, Kim S. Numerical investigation of the pressure effect on the NOx formation in a lean-premixed gas turbine combustor. Energy & Fuels 2021;35(8):6776–84. http://dx.doi.org/10.1021/acs.energyfuels.0c02909.

[15] Mashruk S, Shi H, Mazzotta L, Ustun CE, Aravind B, Meloni R, Alnasif A, Boulet E, Jankowski R, Yu C, Alnajideen M, Paykani A, Maas U, Slefarski R, Borello D, Valera-Medina A. Perspectives on NO_x emissions and impacts from ammonia combustion processes. Energy & Fuels 2024;38(20):19253–92. http://dx.doi.org/10.1021/acs.energyfuels.4c03381.

[16] Savarese M, Giuntini L, Malpica Galassi R, Iavarone S, Galletti C, De Paepe W, Parente A. Model-to-model Bayesian calibration of a chemical reactor network for pollutant emission predictions of an ammonia-fuelled multistage combustor. IJHE 2023.

[17] Rasmussen CE. Gaussian processes in machine learning. In: Bousquet O, von Luxburg U, Rätsch G, editors. Advanced lectures on machine learning: ML summer schools 2003, canberra, Australia, February 2 - 14, 2003, tübingen, Germany, August 4 - 16, 2003, revised lectures. Berlin, Heidelberg: Springer Berlin Heidelberg; 2004, p. 63–71. http://dx.doi.org/10.1007/978-3-540-28650-9_4.

[18] Donato L, Kamal MM, Procacci A, Cafiero M, Sharma S, Galletti C, Coussement A, Parente A. Integrating data assimilation and sparse sensing for updating a digital twin of a semi-industrial furnace. Proc Combust Inst 2024;40(1):105284. http://dx.doi.org/10.1016/j.proci.2024.105284, URL https://www.sciencedirect.com/science/article/pii/S1540748924000944.

[19] Peherstorfer B, Willcox K, Gunzburger M. Survey of multifidelity methods in uncertainty propagation, inference, and optimization. SIAM Rev 2018;60(3):550–91. http://dx.doi.org/10.1137/16M1082469.

[20] Han Z-H, Zimmermann, Görtz S. Alternative cokriging method for variable-fidelity surrogate modeling. AIAA J 2012;50(5):1205–10. http://dx.doi.org/10.2514/1.J051243.

[21] Perron C, Rajaram D, Mavris D. Development of a multi-fidelity reduced-order model based on manifold alignment. In: AIAA Aviation 2020 forum. http://dx.doi.org/10.2514/6.2020-3124.

[22] Özden A, Savarese M, Giuntini L, Procacci A, Malpica Galassi R, Coussement A, Contino F, Parente A. A multi-fidelity framework for developing digital twins of combustion systems from heterogeneous data: Application to ammonia combustion. Proc Combust Inst 2024;40(1):105608. http://dx.doi.org/10.1016/j.proci.2024.105608, URL https://www.sciencedirect.com/science/article/pii/S1540748924004164.

[23] Ghanem RG, Spanos PD. Stochastic finite elements: A spectral approach. New York, NY: Springer; 1990.

[24] Le Maitre O, Knio OM. Spectral methods for uncertainty quantification: With applications to computational fluid dynamics. New York: Springer Science & Business Media; 2010, http://dx.doi.org/10.1007/978-90-481-3520-2.

[25] Amaduzzi R, Bertolino A, Özden A, Galassi RM, Parente A. Impact of scalar mixing uncertainty on the predictions of reactor-based closures: Application to a lifted methane/air jet flame. Proc Combust Inst 2023;39(4):5165–75. http://dx.doi.org/10.1016/j.proci.2022.06.028, URL https://www.sciencedirect.com/science/article/pii/S1540748922000396.

[26] Somarathne KDKA, Hatakeyama S, Hayakawa A, Kobayashi H. Numerical study of a low emission gas turbine like combustor for turbulent ammonia/air premixed swirl flames with a secondary air injection at high pressure. Int J Hydrog Energy 2017;42(44):27388–99. http://dx.doi.org/10.1016/j.ijhydene.2017.09.089, URL https://www.sciencedirect.com/science/article/pii/S0360319917337515.

[27] Okafor EC, Somarathne KA, Hayakawa A, Kudo T, Kurata O, Iki N, Kobayashi H. Towards the development of an efficient low-NO_x ammonia combustor for a micro gas turbine. Proc Combust Inst 2019;37(4):4597–606. http://dx.doi.org/10.1016/j.proci.2018.07.083, URL https://www.sciencedirect.com/science/article/pii/S1540748918305017.

[28] Piscopo A, De Paepe W, Parente A, Iavarone S. Chemical timescale analysis of the partially stirred reactor model for a hydrogen-fuelled scramjet. Results Eng 2024;23:102834. http://dx.doi.org/10.1016/j.rineng.2024.102834, URL https://www.sciencedirect.com/science/article/pii/S2590123024010892.

[29] Shrestha KP, Seidel L, Zeuch T, Mauss F. Detailed kinetic mechanism for the oxidation of ammonia including the formation and reduction of nitrogen oxides. Energy & Fuels 2018;32(10):10202–17. http://dx.doi.org/10.1021/acs.energyfuels.8b01056.

[30] Bordbar H, Fraga GC, Hostikka S. An extended weighted-sum-of-gray-gases model to account for all CO_2-H_2O molar fraction ratios in thermal radiation. Int Commun Heat Mass Transfer 2020;110:104400. http://dx.doi.org/10.1016/j.icheatmasstransfer.2019.104400, URL https://www.sciencedirect.com/science/article/pii/S0735193319302660.

[31] Okafor EC, Tsukamoto M, Hayakawa A, Somarathne KKA, Kudo T, Tsujimura T, Kobayashi H. Influence of wall heat loss on the emission characteristics of premixed ammonia-air swirling flames interacting with the combustor wall. Proc Combust Inst 2021;38(4):5139–46. http://dx.doi.org/10.1016/j.proci.2020.06.142, URL https://www.sciencedirect.com/science/article/pii/S1540748920302224.

[32] Jottrand S, Hendrick P. Centrifugal compressor preliminary design optimization for a hydrogen pipeline compression station. In: Turbo Expo: Power Land, Sea, Air. Volume 2: Ceramics and Ceramic Composites; Coal, Biomass, Hydrogen, and Alternative Fuels. 2024, http://dx.doi.org/10.1115/GT2024-123827, V002T03A010.

[33] Eurostat. Development of electricity prices for household consumers (2008–2024). 2024, URL: https://ec.europa.eu/eurostat/statistics-explained/index.php?title=File:Development_of_electricity_prices_for_household_consumers_2008-2024.png (Accessed: 13 December 2024).

[34] Verleysen K, Coppitters D, Parente A, Contino F. Where to build the ideal solar-powered ammonia plant? Design optimization of a Belgian and Moroccan power-to-ammonia plant for covering the Belgian demand under uncertainties. Appl Energy Combust Sci 2023;14:100141. http://dx.doi.org/10.1016/j.jaecs.2023.100141, URL https://www.sciencedirect.com/science/article/pii/S2666352X23000304.

[35] Hydrogen council, hydrogen insights 2023 december update. 2023, Hydrogen Council, Available at: https://hydrogencouncil.com/en/hydrogen-insights-2023-december-update/.

[36] Kobayashi H, Hayakawa A, Somarathne KKA, Okafor EC. Science and technology of ammonia combustion. Proc Combust Inst 2019;37(1):109–33. http://dx.doi.org/10.1016/j.proci.2018.09.029, URL https://www.sciencedirect.com/science/article/pii/S1540748918306345.

[37] García-Ruiz P, Castejón D, Abengochea M, Bilbao R, Alzueta MU. High-pressure study of the conversion of NH_3/H_2 mixtures in a flow reactor. Proc Combust Inst 2024;40(1):105726. http://dx.doi.org/10.1016/j.proci.2024.105726, URL https://www.sciencedirect.com/science/article/pii/S1540748924005340.